

Deep-learning-assisted detection and termination of spiral- and broken-spiral waves in mathematical models for cardiac tissue

Mahesh Kumar Mulimani,^{1,*} Jaya Kumar Alageshan,^{1,†} and Rahul Pandit^{1,‡}

¹*Centre for Condensed Matter Theory, Department of Physics,
Indian Institute of Science, Bangalore 560012, India.*

Unbroken and broken spiral waves, in partial-differential-equation (PDE) models for cardiac tissue, are the mathematical analogs of life-threatening cardiac arrhythmias, namely, ventricular tachycardia (VT) and ventricular-fibrillation (VF). We develop a (a) deep-learning method for the detection of unbroken and broken spiral waves and (b) the elimination of such waves, e.g., by the application of low-amplitude control currents in the cardiac-tissue context. Our method is based on a convolutional neural network (CNN) that we train to distinguish between patterns with spiral waves \mathcal{S} and without spiral waves $\mathcal{N}\mathcal{S}$. We obtain these patterns by carrying out extensive direct numerical simulations (DNSs) of PDE models for cardiac tissue in which the transmembrane potential V , when portrayed via pseudocolor plots, displays patterns of electrical activation of types \mathcal{S} and $\mathcal{N}\mathcal{S}$. We then utilise our trained CNN to obtain, for a given pseudocolor image of V , a heat map that has high intensity in the regions where this image shows the cores of spiral waves. Given this heat map, we show how to apply low-amplitude Gaussian current pulses to eliminate spiral waves efficiently. Our *in silico* results are of direct relevance to the detection and elimination of these arrhythmias because our elimination of unbroken or broken spiral waves is the mathematical analog of low-amplitude defibrillation.

PACS numbers: 87.19.Xx, 87.15.Aa

The normal pumping of blood by mammalian hearts is initiated by electrical waves of excitation that propagate through cardiac tissue and induce cardiac contractions. The abnormal propagation of such waves can lead to cardiac arrhythmias, like ventricular tachycardia (VT) and ventricular fibrillation (VF), which cause sudden cardiac death (SCD) that is among the leading causes of death in the industrialised world [1–3] (see, e.g., Refs. [4, 5] for SCD data from India and the USA). The principal cause of VT and VF are spiral or scroll waves of electrical activation in cardiac tissue; unbroken (broken) spiral or scroll waves are associated with VT (VF). Such waves have been studied *in vivo* [6–8] in mammalian hearts, *in vitro* [9–12] in cultures of cardiac myocytes, and *in silico* [13–15], in mathematical models for cardiac tissue. The efficient elimination of such spiral or scroll waves and the subsequent restoration of the normal rhythm of a mammalian heart, is a difficult problem; this can be attempted by pharmacological means [16] or by electrical means called *defibrillation* [17]. Defibrillation by the application of low-amplitude current pulses is the grand-challenge here [18]. Two important steps are required for such defibrillation: (a) An efficient detection of spiral waves or their broken-wave forms; (b) the elimination of such waves by low-amplitude electrical pulses [13–15, 17] or through optogenetic methods [19].

We develop a deep-learning method, based on a convolutional neural network (CNN), that helps us to ac-

complish task (a). We then develop the mathematical analog of a defibrillation scheme for the efficient elimination of well-formed spiral and broken spiral waves in two dimensions (2D). We note, in passing, that electrical waves in cardiac tissue belong to a large class of nonlinear waves in excitable media, e.g., calcium-ion waves in *Xenopus* oocytes [20], waves in chemical reactions of the Belousov-Zhabotinsky type [21], waves that occur during the oxidation of carbon monoxide on the surface of platinum [22–24], excitable-wave patterns in a recent semiconductor-laser experiment [25], and waves in *dictyostelium discoideum* that are associated with the cyclic-AMP signalling [26, 27]; our step (a) can be applied, *mutatis mutandis*, for the detection of spiral waves in such systems.

Specifically, we *train* our CNN to *classify*, into the following two sets, patterns of electrical-wave activation, which we obtain from *in silico* studies of different mathematical models for cardiac tissue [28–32]: (a) spiral waves (\mathcal{S}); and (b) no spiral waves ($\mathcal{N}\mathcal{S}$) (Fig. 1). Next, we use our trained CNN to detect spiral-wave patterns, with both unbroken and broken spirals. We then use the outputs from our CNN to construct a *heat map* that has high intensity in the regions with spiral cores. We demonstrate how to eliminate the broken or unbroken spiral waves by applying low-amplitude current stimuli at those positions at which the heat map has high intensity; this is the mathematical analog of *defibrillation* [17].

* maheshk@iisc.ac.in ; contributed to all aspects of this study

† jayaka@iisc.ac.in ; contributed to all aspects of this study

‡ rahul@iisc.ac.in;

also at Jawaharlal Nehru Centre For Advanced Scientific Research, Jakkur, Bangalore, India

Mathematical models for cardiac tissue use nonlinear partial differential equations (PDEs) of the reaction-

diffusion type given below:

$$\frac{\partial V}{\partial t} = D_0 \nabla^2 V + f(V, g); \quad \frac{\partial g}{\partial t} = \epsilon(V, g)h(V, g); \quad (1)$$

$$\frac{\partial V}{\partial t} = D_0 \nabla^2 V - \frac{I_{ion}}{C_m}; \quad I_{ion} = \sum_i I_i. \quad (2)$$

We use two classes of models, namely, (a) two-variable models [Eq.(1)] and (b) biologically realistic models with ion channels, ion pumps, and ion exchangers [Eq.(2)]. The type-(a) models that we work with are (i) the Barkley model [28] and (ii) the Aliev-Panfilov model [29], in which V , g , and D_0 are, respectively, the transmembrane potential, the effective ionic gate (a slow variable), and the diffusion constant; f and h are nonlinear functions of V and g . We employ the following type-(b) models: (i) the Luo-Rudy phase-I (LR-I) guinea-pig-ventricular model [30]; (ii) the TP06 human-ventricular model [31]; and (iii) the O'Hara-Rudy (ORd) human-ventricular model [32], where V , I_i , and C_m are the transmembrane potential, the ionic current for ion-channel i , and the membrane capacitance, respectively (see the Supplemental Material [?] for the forms of f , h , and I_i in these models). We use the forward-Euler method (step size Δt) for time marching, and a finite-difference scheme in space (step size Δx), with a 5-point stencil for the Laplacian, and no-flux boundary conditions to obtain numerical solutions of Eqs. (1) and (2), in two-dimensional (2D) square domains with $N \times N$ grid points, with $128 \leq N \leq 1024$; in most of our simulations we use $N = 512$. We choose Δt and Δx such that the von-Neumann stability criterion is satisfied [33]. We focus on electrical activity in cardiac tissue, so, from our numerical solutions of these PDEs, we extract the spatiotemporal evolution of V , which yields several patterns like *spiral waves* (Fig.1(a)), *target waves* (top right corner in Fig.1(b)), *plane waves* (bottom left corner in Fig.1(b)), and states with *spiral break-up* (Fig.3(a)).

In Fig. 1 we show representative pseudocolor images of V that we obtain from our numerical solutions of Eqs. (1) and (2) over a wide range of parameters in the cardiac-tissue models that we have listed above. We use 22,000 such images to train, and then test, our CNN. We create additional images by performing geometrical operations on the primary pseudocolor images V , e.g., inequivalent reflections about the horizontal and vertical axes, so that our dataset of images is not biased in favor of any particular orientation; this improves the training performance of our CNN. We train our CNN with 70% of the total number of images; and we save the remaining 30% of the images for the validation of our CNN model.

Our solutions of Eqs. (1) or (2) yield V at N^2 grid points. We first define the normalised transmembrane potential $\tilde{V} = (V - V_{min}) / (V_{max} - V_{min})$; V_{max} and V_{min} are, respectively, the maximal and minimal values of V , so $0 \leq \tilde{V} \leq 1$. We then reduce the large number of grid points by specifying \tilde{V} on 32×32 points by using the *resize* function in MATLAB R2018b. We use the Deep Learning Toolbox in MATLAB R2018b to develop our

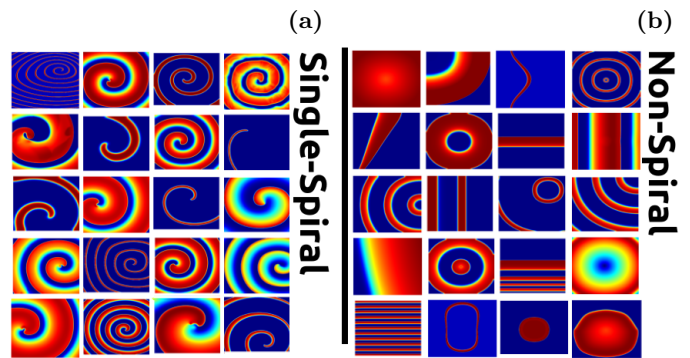


FIG. 1. Collages of illustrative pseudocolor plots of V with (a) single-spiral (\mathcal{S}) images and (b) no spiral ($\mathcal{N}\mathcal{S}$) images, which we use for training our CNN. In (a), the arm-width of the spiral and its rotation frequency depends on the model [Eqs. (1) or (2)] and the parameters therein; the spiral-wave-initiation scheme controls the chirality of the spiral and the position of its core. In (b), the $\mathcal{N}\mathcal{S}$ class includes plane waves and target waves.

CNN, which we depict schematically in Fig. 2. It has three main layers: (1) *Input*; (2) *Middle*; and (3) *Final*. The Middle layer contains three sets of *Convolution*, *Rectified Linear Unit* (ReLU), and *MaxPool* sub-layers. The Final layer contains two fully connected *Artificial Neural Networks* (ANNs). We give a brief description of the implementation of our CNN in the Supplemental Material [?].

We begin the training by feeding the the image of \tilde{V} to our CNN. If the CNN output predicts the class of the input image incorrectly, then we use a proxy cost function to rectify this error iteratively (until the CNN yields the correct output class). Specifically, we achieve this for our CNN by minimizing the cross-entropy cost function

$$\mathcal{C} = - \sum_{\ell=1}^M \sum_{q=0}^{\eta-1} \frac{[O_{\ell,q} \ln(\tilde{O}_{\ell,q}) + (1 - O_{\ell,q}) \ln(1 - \tilde{O}_{\ell,q})]}{M}, \quad (3)$$

by using the stochastic-gradient-descent method with a learning rate $\alpha = 0.001$ (see, e.g., Chapter 2 of Ref [34]); here, $\tilde{O}_{\ell,q}$ are the CNN outputs ($\tilde{O}_{\ell,q} \in (0, 1)$) and $O_{\ell,q}$ are the real outputs, for the input image ℓ , and M is the *mini-batch* size (the total number of images is divided into subsets, called mini-batches, with M images each); we use $M = 128$. For the class \mathcal{S} , $O_{\ell,0} = 1$ and $O_{\ell,1} = 0$; and for $\mathcal{N}\mathcal{S}$, $O_{\ell,0} = 0$ and $O_{\ell,1} = 1$.

Even though we train our CNN with single-spiral-wave patterns, it manages to identify patterns with broken spiral waves as belonging to the class \mathcal{S} : We have checked that this CNN classifies 10,000 broken-spiral-wave patterns (see the pseudocolor plot of V in Fig.3 (a)) as \mathcal{S} , with an accuracy of 99.6%. This is especially useful when we carry out the mathematical analog of defibrillation, i.e., the elimination of all spirals, unbroken or broken. We can, indeed, utilise our trained CNN to examine pseudocolor plots of V , during our numerical simulation of a mathematical model for cardiac tissue; the moment this

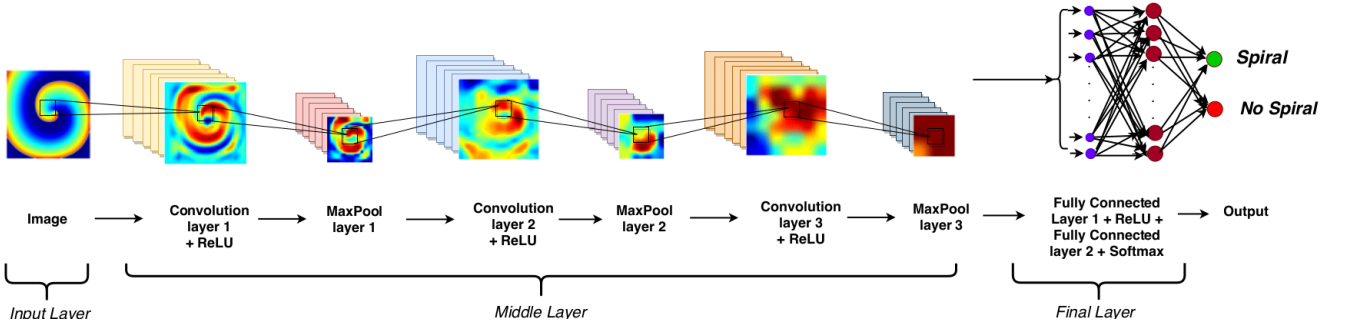


FIG. 2. A schematic diagram of our CNN showing the Input, Middle, and Final layers; the details of each one of these layer are given in the Supplemental Material [?].

CNN detects a pattern of type \mathcal{S} , we can eliminate it by the application of suitable currents on a coarse, control mesh [17] or by using an optogenetics-based control [19] method (we give a brief description of these control methods (see Fig. S3) in the Supplemental Material [?]). Here, we discuss a new scheme for eliminating both broken and unbroken spiral waves; this relies on developing a *heat map*, from a pseudocolor plot of V , for those images that are identified by our CNN to lie in the class \mathcal{S} . This heat map (Fig. 3 (b)) is

$$\mathcal{H}(i, j) = \frac{N_p}{N} \sum_{r=1}^{N/N_p} \text{CNN}(\chi_{i,j}^r \{V\}), \quad (4)$$

$\forall i, j \in \{1, 2, \dots, N\}$; the arguments of the matrix-resizing function $\chi_{i,j}^r$ (a standard function in Matlab) are the $32r \times 32r$ values of V in a square of side $32r$ centred at the point (i, j) , with $1 \leq i, j \leq N$ and $1 \leq r \leq (N/N_p)$; for the images we employ, $N = 512$ and $N_p = 32$. We use the resized $\chi_{i,j}^r$, an image with $N_p \times N_p$ pixels, as an input into our CNN (Fig. 2) and its output, 0 (for $\mathcal{N}\mathcal{S}$) or 1 (for \mathcal{S}), is summed over r to obtain $\mathcal{H}(i, j)$ for a given input pseudocolor plot of V . Clearly, $\mathcal{H}(i, j) \in [0, 1]$; and it is large if there is a spirale core near the point (i, j) . In the left and right panels of Fig. 3 we depict, respectively, a pseudocolor plot of V , with a broken-spiral-wave pattern, and the corresponding heat map. We now show how to use such a heat map to develop a new control scheme for the elimination of both broken and unbroken spiral waves.

Spiral-wave excitations emanate from the spiral core, so we might expect that the elimination of this core could lead to the removal of the spiral wave. However, when we apply a current pulse on a disk centred at the spiral core, we find that it leads to the formation of multiple spiral cores along the boundary of the disk. We prevent the formation of such multiple spiral cores as follows: We first show, for a single spiral wave in the Aliev-Panfilov model, that, by applying a current pulse with a spatial profile that is a symmetrical, two-dimensional (2D) Gaussian (centred at the spiral core, with equal widths in both x and y directions $\sigma_x = \sigma_y = \sigma$, and with a peak intensity of I_{def}), we can remove the core and the wave *without*

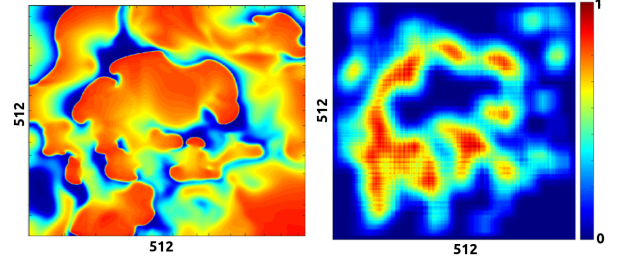


FIG. 3. Pseudocolor plots of (left panel) V , showing broken spiral waves, and (right panel) the heat map \mathcal{H} for the image in the left panel (see text).

forming multiple spiral cores (Fig. 4). Henceforth, we refer to such a current profile as a Gaussian current pulse with width σ .

We now consider a pattern with multiple spiral waves (e.g., the pseudocolor plot of V in the left panel of Fig. 3), whose spatial extent is much smaller than the large spiral wave in Fig. 4. We consider a square lattice of points, labelled by (i', j') , with $0 \leq i', j' \leq N_G$, i.e., the side of the unit cell $a = N_G \Delta x$ (cm). On each of these points we impose a Gaussian current pulse $G(i', j')$ of width σ and amplitude I_{def} ; the total, normalised contribution of these pulses, at the point (i, j) , with $0 \leq i, j \leq (N - 1)$, in the original image, is

$$\tilde{\mathcal{G}}(i, j) = \sum_{i', j'=0}^{N} G\left(i - i' \frac{N}{N_G}, j - j' \frac{N}{N_G}\right); \quad (5)$$

$$\mathcal{G}(i, j) = \tilde{\mathcal{G}}(i, j) / [\tilde{\mathcal{G}}_{max}];$$

here, $\tilde{\mathcal{G}}_{max} = \max_{(i,j)}[\tilde{\mathcal{G}}(i, j)]$. The final current pulse that we apply, for a time t_{def} ms at the point (i, j) , is given by the Hadamard product

$$\mathcal{P}_{\mathcal{H}}(i, j) = I_{def} \mathcal{H}(i, j) \mathcal{G}(i, j), \quad (6)$$

where I_{def} sets the scale of the current that is applied. Multiple spiral waves are eliminated by the application of $\mathcal{P}_{\mathcal{H}}(i, j)$ (henceforth, Gaussian-control scheme) as we demonstrate below.

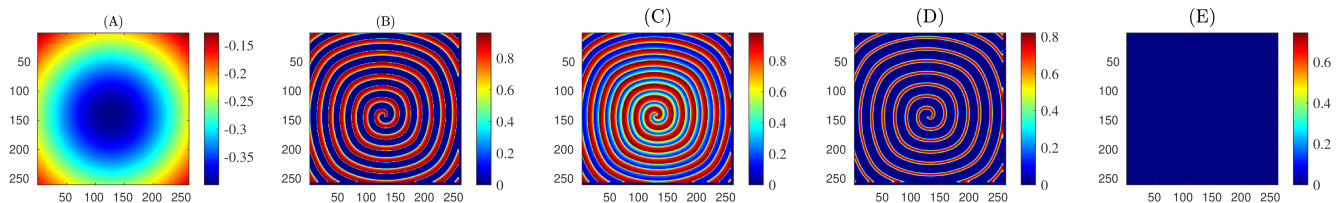


FIG. 4. Pseudocolor plots which shows, (A) the defibrillation current as $\mathcal{P}_{\mathcal{H}}$ (single 2D Gaussian centered at the spiral core), whose $I_{def} = 0.5$ pA/pF, $\sigma = 0.375N\Delta x$ (cm) and $N = 256$. (B)-(F) V of the Aliev-Panfilov model (Ref [29]). (B) the spiral wave before application of the defibrillation current and (C) shows the time of application and (D)-(F) After the defibrillation current is applied. We observe that spiral wave is eliminated after the application of the defibrillation current of 2D Gaussian profile.

In Figs. 5 (A) and (B), we show illustrative pseudocolor plots of, respectively, V and its heat map \mathcal{H} (Eq.(4)), for an image with a broken spiral wave, in the TP06 model. Figures 5 (C) and (D) depict, respectively, pseudocolor plots of the summed and normalised 2D Gaussians ($\mathcal{G}(i, j)$ in Eq.(5)) and the Hadamard product $\mathcal{P}_{\mathcal{H}}(i, j)$ (with $I_{def} = 1$ pA/pF in Eq.(6)). Our Gaussian-control scheme is illustrated by the pseudocolor plots of V [Figs. 5 (E)-(H)]; these show the spatiotemporal evolution of V after the application of $\mathcal{P}_{\mathcal{H}}(i, j)$, which is turned off at $t = t_{def}$ (for the complete spatiotemporal evolution see the video V1 in the Supplemental Material [?]). In Figs. 5 (I)-(L) we show the counterparts of Figs. 5 (E)-(H) for the control scheme in which a current pulse is applied on a square mesh to eliminate broken spiral waves (see Refs. [13–15, 17], the Supplemental Material [?], and the video V2); we refer to this as the mesh-control scheme.

Control scheme	N_G	a (cm)	σ (cm)	I_{def} (pA/pF)	t_{def} (ms)
GC1	64	1.6	$0.37 a$	5	120
GC2	96	2.4	$0.37 a$	5	120
MC	64	-	-	15	120

TABLE I. The parameter values that we use for our Gaussian-control (GC1 and GC2) and Mesh-control (MC) schemes in our illustrative simulations.

The efficacy of our Gaussian-control scheme depends on the parameters a , σ , I_{def} , and t_{def} . We list these parameters (Table I) for two illustrative Gaussian-control runs, GC1 and GC2, and one run, MC, in which we use a mesh-control scheme, for the TP06 model. By comparing the results of such runs we find that, for large values of a , our Gaussian-control scheme is not successful in removing spiral waves; e.g., in the TP06 model, broken spiral waves are suppressed for the value of a that we use in run GC1, but not for the value of a in run GC2 (Table I). For the parameters in run GC1, Figs. 5 (M)-(P) show phase diagrams, in the (t_{def}, σ) plane and for representative values of I_{def} , with parameter regions in which our Gaussian-control scheme succeeds (red) and does not

succeed (blue) in controlling broken spiral waves: This Gaussian-control scheme also eliminates broken and unbroken spiral waves in all the other cardiac-tissue models that we have studied (see Figs. S5 and S6 in the Supplemental Material [?]).

By comparing the pseudocolor plots in rows two and three of Fig. 5, we can contrast the effectiveness of our Gaussian-control scheme with that of the mesh-control scheme of Refs [17]. We find, in particular, that our Gaussian-control scheme eliminates broken spiral waves with $I_{def} = 5$ pA/pF; by contrast, the mesh scheme requires $I_{def} = 15$ pA/pF for such elimination. Thus, the Gaussian-control scheme leads to the elimination of spiral waves with lower local currents than the mesh-control scheme, with all other parameters held fixed.

We have checked that our CNN can be used to detect scroll waves in three-dimensional(3D) simulation domains (see Fig. S4 of the Supplementary Material Ref [?]). The elimination of such 3D scroll waves by the application of currents on a 2D surface of a 3D domain remains a significant challenge Ref. [13–15, 17].

Our deep-learning-assisted Gaussian-control method is an important step in the detection and elimination of both broken and unbroken spiral waves. Machine-learning techniques have been used, e.g., in Refs. [35–37], for the effective detection of anomalies in electrocardiograms (ECGs), which can then be eliminated by the controlled delivery of electrical signals via automated defibrillators (see, e.g. Refs. [35, 38, 39]). To the best of our knowledge, no machine-learning method has been employed so far for the detection of spiral waves in, e.g., pseudocolor plots of V . Our study uses the complete spatial information in patterns of V to develop an efficient Gaussian-control scheme for the elimination of unbroken and broken spiral waves, which are the mathematical analogs of life-threatening VT and VF [13–15].

We hope that our CNN-based detection of spiral waves and our Gaussian-control scheme will be tested in *in-vitro* experiments with cardiac myocytes, such as those used in the studies of Refs. [9–12, 19, 40, 41]. Our CNN can also be used to detect spiral waves in other excitable media [20–27].

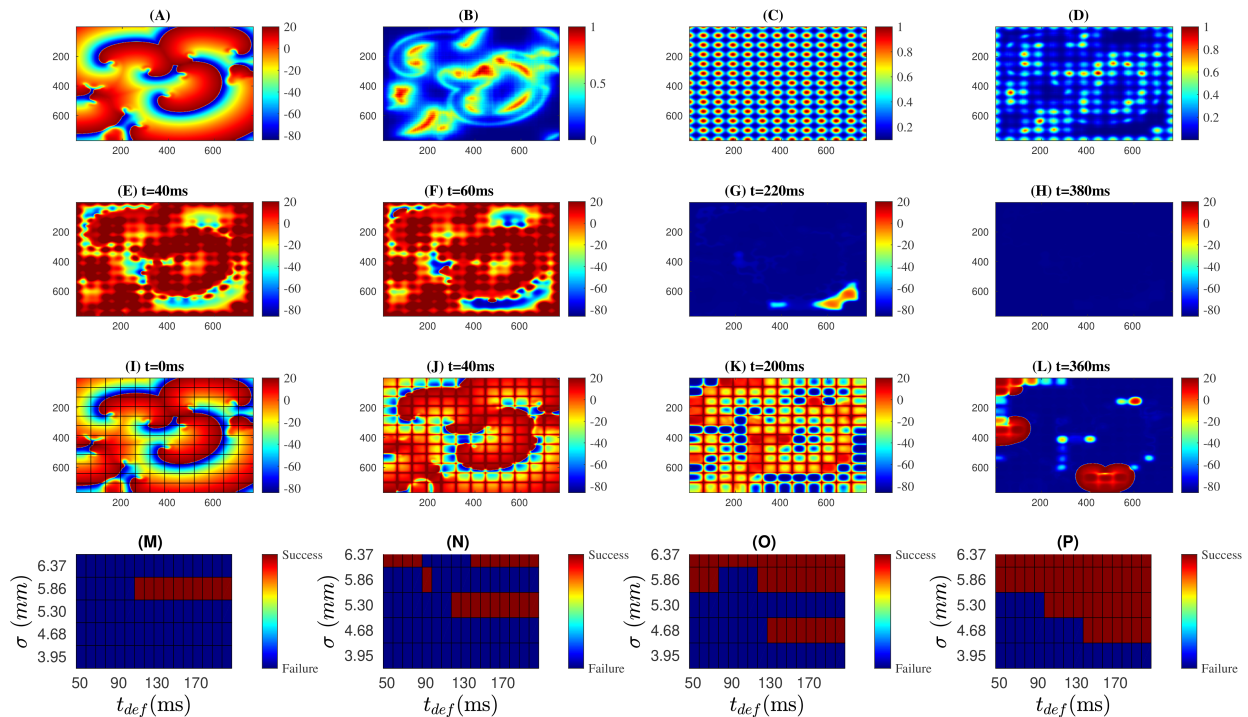


FIG. 5. Pseudocolor plots of (A) V , for an illustrative, broken spiral wave from our simulation of the TP06 model, (B) the corresponding heat map \mathcal{H} (Eq. 4), (C) the summed and normalised 2D Gaussians ($\mathcal{G}(i, j)$ in Eq. 5), and (D) the Hadamard product $\mathcal{P}_{\mathcal{H}}(i, j)$ (with $I_{def} = 1$ pA/pF in Eq. 6). (E)-(H): Pseudocolor plots of V , at different representative times, showing the elimination of the broken spiral waves (as in (A) at $t = 0$) after the application of $\mathcal{P}_{\mathcal{H}}(i, j)$; $\mathcal{P}_{\mathcal{H}}(i, j)$ is turned off at $t = t_{def} = 120$ ms (for the complete spatiotemporal evolution see the video V1 in the Supplemental Material [?]). (I)-(L): the analogs of (E)-(H) for the current-mesh control scheme of Refs. [17] (see the video V2 in Supplemental Material [?]). Phase diagrams in the (t_{def}, σ) plane showing parameter regions in which our Gaussian control scheme [(E)-(F)] succeeds (red) and does not succeed (blue) in controlling broken spiral waves for (M) $I_{def} = 5$ pA/pF, (N) $I_{def} = 10$ pA/pF, (O) $I_{def} = 15$ pA/pF and (P) $I_{def} = 20$ pA/pF.

ACKNOWLEDGMENTS

We thank DST, CSIR, UGC (India) for the support

and the Supercomputer Education and Research Centre (SERC, IISc) for computational resources.

-
- [1] R. Mehra, *Journal of electrocardiology* **40**, S118 (2007).
[2] R. Majumder, A. R. Nayak, and R. Pandit, *An Overview of Spiral- and Scroll-Wave Dynamics in Mathematical Models for Cardiac Tissue* (Springer Berlin Heidelberg, Berlin, Heidelberg, 2011), pp. 269–282, ISBN 978-3-642-17575-6, URL https://doi.org/10.1007/978-3-642-17575-6_14.
[3] R. Clayton, O. Bernus, E. Cherry, H. Dierckx, F. H. Fenton, L. Mirabella, A. V. Panfilov, F. B. Sachse, G. Seemann, and H. Zhang, *Progress in biophysics and molecular biology* **104**, 22 (2011).
[4] B. S. Honnekeri, D. Lokhandwala, G. K. Panicker, and Y. Lokhandwala, *J Assoc Physicians India* **62**, 36 (2014).
[5] Z.-J. Zheng, J. B. Croft, W. H. Giles, and G. A. Mensah, *Circulation* **104**, 2158 (2001).
[6] C. I. Berul, M. J. Aronovitz, P. J. Wang, and M. E. Mendelsohn, *Circulation* **94**, 2641 (1996).
[7] M. Chinushi, D. Kozhevnikov, E. B. Caref, M. Restivo, and N. El-Sherif, *Journal of cardiovascular electrophysiology* **14**, 632 (2003).
[8] A. R. Gelzer, M. L. Koller, N. F. Otani, J. J. Fox, M. W. Enyeart, G. J. Hooker, M. L. Riccio, C. R. Bartoli, and R. F. Gilmour, *Circulation* **118**, 1123 (2008).
[9] J. M. Davidenko, P. F. Kent, D. R. Chialvo, D. C. Michaels, and J. Jalife, *Proceedings of the National Academy of Sciences* **87**, 8785 (1990).
[10] T. Ikeda, T. Uchida, D. Hough, J. J. Lee, M. C. Fishbein, W. J. Mandel, P.-S. Chen, and H. S. Karagueuzian, *Circulation* **94**, 1962 (1996).
[11] M. Valderrábano, Y.-H. Kim, M. Yashima, T.-J. Wu, H. S. Karagueuzian, and P.-S. Chen, *Journal of the American College of Cardiology* **36** (2000).
[12] Z. Y. Lim, B. Maskara, F. Aguel, R. Emokpae, and L. Tung, *Circulation* **114**, 2113 (2006).

- [13] T. Shajahan, S. Sinha, and R. Pandit, *Physical Review E* **75**, 011929 (2007).
- [14] T. Shajahan, A. R. Nayak, and R. Pandit, *PLoS One* **4**, e4738 (2009).
- [15] A. R. Nayak and R. Pandit, *Frontiers in physiology* **5**, 207 (2014).
- [16] J. Moreno, P.-C. Yang, J. Bankston, E. Grandi, D. Bers, R. Kass, and C. Clancy, *Circulation research* pp. CIRCRESAHA-113 (2013).
- [17] S. Sinha, A. Pande, and R. Pandit, *Physical review letters* **86**, 3678 (2001).
- [18] S. Luther, F. H. Fenton, B. G. Kornreich, A. Squires, P. Bittihn, D. Hornung, M. Zabel, J. Flanders, A. Gladuli, L. Campoy, et al., *Nature* **475**, 235 (2011).
- [19] B. O. Bingen, M. C. Engels, M. J. Schali, W. Jangsangthong, Z. Neshati, I. Feola, D. L. Ypey, S. F. Askar, A. V. Panfilov, D. A. Pijnappels, et al., *Cardiovascular research* **104**, 194 (2014).
- [20] J. Lechleiter, S. Girard, E. Peralta, and D. Clapham, *Science* **252**, 123 (1991).
- [21] A. T. Winfree, *Science* **175**, 634 (1972).
- [22] M. Falcke, M. Bär, H. Engel, and M. Eiswirth, *The Journal of chemical physics* **97**, 4555 (1992).
- [23] R. Imbihl and G. Ertl, *Chemical Reviews* **95**, 697 (1995).
- [24] A. Pande and R. Pandit (1999).
- [25] F. Marino and G. Giacomelli, *Physical Review Letters* **122**, 174102 (2019).
- [26] J. J. Tyson and J. Murray, *Development* **106**, 421 (1989).
- [27] J. Rietdorf, F. Siegert, and C. J. Weijer, *Developmental biology* **177**, 427 (1996).
- [28] D. Barkley, *Physica D: Nonlinear Phenomena* **49**, 61 (1991).
- [29] R. R. Aliev and A. V. Panfilov, *Chaos, Solitons & Fractals* **7**, 293 (1996).
- [30] C.-h. Luo and Y. Rudy, *Circulation research* **68**, 1501 (1991).
- [31] K. H. Ten Tusscher and A. V. Panfilov, *American Journal of Physiology-Heart and Circulatory Physiology* **291**, H1088 (2006).
- [32] T. O'Hara, L. Virág, A. Varró, and Y. Rudy, *PLoS computational biology* **7**, e1002061 (2011).
- [33] W. H. Press, S. A. Teukolsky, W. T. Vetterling, and B. P. Flannery, *Numerical recipes 3rd edition: the art of scientific computing* (2007).
- [34] M. A. Nielsen, *Neural networks and deep learning*, vol. 25 (Determination press USA, 2015).
- [35] C. Figuera, U. Irusta, E. Morgado, E. Aramendi, U. Ayala, L. Wik, J. Kramer-Johansen, T. Eftestøl, and F. Alonso-Atienza, *PloS one* **11**, e0159654 (2016).
- [36] L. Maršánová, M. Ronzhina, R. Smíšek, M. Vitek, A. Němcová, L. Smital, and M. Nováková, *Scientific reports* **7**, 11239 (2017).
- [37] A. Y. Hannun, P. Rajpurkar, M. Haghpanahi, G. H. Tison, C. Bourn, M. P. Turakhia, and A. Y. Ng, *Nature medicine* **25**, 65 (2019).
- [38] S. Singh, S. K. Pandey, U. Pawar, and R. R. Janghel, *Procedia Computer Science* **132**, 1290 (2018).
- [39] S. C. Ao Li and J. M. R., *Res Med Eng Sci.* **4**(4). RMES.000592.2018.DOI: 10.31031/RMES.2018.04.000592 (????).
- [40] T. Shajahan, S. Berg, S. Luther, V. Krinski, and P. Bittihn, *New Journal of Physics* **18**, 043012 (2016).
- [41] N. Kudryashova, V. Tsvelaya, K. Agladze, and A. Panfilov, *Scientific reports* **7**, 7887 (2017).

Supplementary Material: Deep-learning-assisted detection and termination of spiral and broken spiral waves in mathematical models for cardiac tissue

Mahesh Kumar Mulimani,^{1,*} Jaya Kumar Alageshan,^{1,†} and Rahul Pandit^{1,‡}

¹*Centre for Condensed Matter Theory, Department of Physics,
Indian Institute of Science, Bangalore 560012, India*

PACS numbers: 87.19.Xx, 87.15.Aa

We provide details of (a) the models we use [Sec. I], (b) our convolutional neural network (CNN) [Sec. II], and (c) some low-amplitude defibrillation (or spiral-removal) schemes [Sec. III] in mathematical models for cardiac tissue.

$$\frac{\partial V}{\partial t} = D_0 \nabla^2 V + f(V, g); \quad (3)$$

$$\frac{\partial g}{\partial t} = h(V, g). \quad (4)$$

(i) *Barkley (B) model*

$$f(V, g) = -\frac{1}{\epsilon_0} V(1-V)(V - V_{thr}(g));$$

$$h(V, g) = V - g;$$

$$\epsilon_0 = \frac{\tau_V}{\tau_g}; V_{thr} = \frac{g+b}{a}.$$

(ii) *Aliev-Panfilov (AP) model*

$$f(V, g) = -kV(V - V_{thr})(V - 1) - Vg;$$

$$h(V, g) = \epsilon(V, g)(-g - kV(V - V_{thr} - 1));$$

$$\epsilon(V, g) = \epsilon_0 + \frac{\mu_1 g}{\mu_2 + V}; \quad \epsilon_0 = \frac{\tau_V}{\tau_g}. \quad (5)$$

Models of Type (b)

$$\frac{\partial V}{\partial t} = D_0 \nabla^2 V - \frac{I_{ion}}{C_m}; \quad I_{ion} = \sum_i I_i \quad (6)$$

We list the currents I_i for all the realistic models we use in Tables S1, S2, and S3. The equations for these currents can be found in Refs. [3–5].

(iii) *Luo-Rudy phase-I (LR-I) model*

I_{Na}	fast inward sodium current
I_{Si}	slow inward calcium current
I_K	Time dependent outward potassium current
I_{K1}	Time independent outward potassium current
I_{Kp}	Plateau outward potassium current
I_b	background current

TABLE S1: **The various ionic currents in the LR-I model; the symbols used for these currents follow Ref. [3].**

I. MODELS

As we have mentioned in the main paper, mathematical models for cardiac tissue use nonlinear partial differential equations (PDEs) of the reaction-diffusion type given below:

$$\frac{\partial V}{\partial t} = D_0 \nabla^2 V + f(V, g); \quad \frac{\partial g}{\partial t} = \epsilon(V, g)h(V, g); \quad (1)$$

$$\frac{\partial V}{\partial t} = D_0 \nabla^2 V - \frac{I_{ion}}{C_m}; \quad I_{ion} = \sum_i I_i. \quad (2)$$

We use two classes of models, namely, (a) two-variable models [Eq.(1)] and (b) biologically realistic models with ion channels, ion pumps, and ion exchangers [Eq.(6)]. The type-(a) models that we work with are (i) the Barkley model [1] and (ii) the Aliev-Panfilov model [2], in which V , g , and D_0 are, respectively, the transmembrane potential, the effective ionic gate (a slow variable), and the diffusion constant; f and h are nonlinear functions of V and g . We employ the following type-(b) models: (i) the Luo-Rudy phase-I (LR-I) guinea-pig-ventricular model [3]; (ii) the TP06 human-ventricular model [4]; and (iii) the O’Hara-Rudy (ORd) human-ventricular model [5], where V , I_i , and C_m are the transmembrane potential, the ionic current for ion-channel i , and the membrane capacitance, respectively. We give the forms of f , h , and I_i in these models below.

Models of Type (a)

*Electronic address: maheshk@iisc.ac.in

†Electronic address: jayaka@iisc.ac.in

‡Electronic address: rahul@iisc.ac.in;

also at Jawaharlal Nehru Centre For Advanced Scientific Research, Jakkur, Bangalore, India

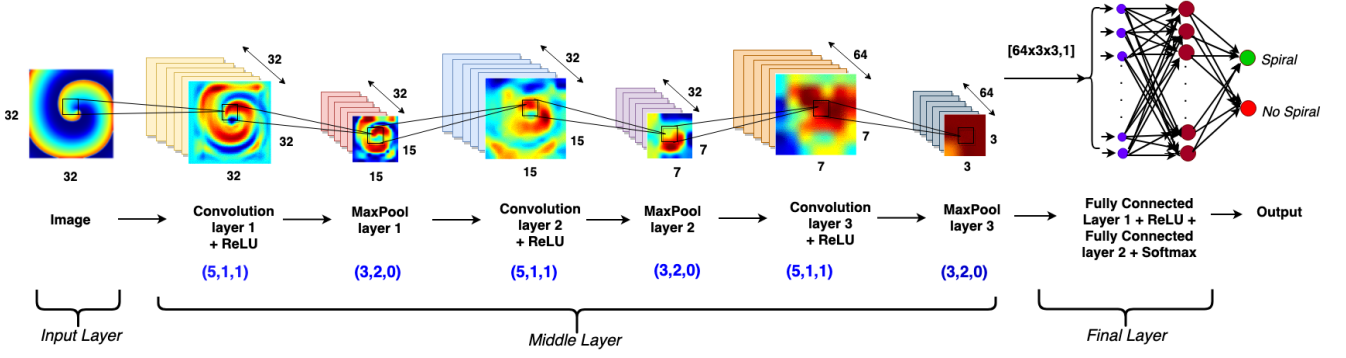


FIG. S1: Schematic diagram of different layers in our CNN: (a) *Input layer*; (b) *Middle layer*; and (c) *Final layer*. The size of the image in each layer is controlled by the *filter size* or *pool size* γ , the *stride length* s , the padding width p , and it is determined by the equation $m = \lfloor (m' - \gamma + 2p)/s \rfloor + 1$, where $m \times m$ is the image size that is the input from the previous layer. Below each layer, we give the values of (γ, s, p) in blue.

(iv) *ten-Tusscher and Panfilov (TP06) model*

I_{Na}	fast inward sodium current
I_{CaL}	L-type inward calcium current
I_{to}	Transient outward current
I_{Ks}	Slow delayed rectifier outward potassium current
I_{Kr}	Rapid delayed rectifier outward potassium current
I_{K1}	Inward rectifier potassium current
I_{NaCa}	Na^+/Ca^{++} exchange current
I_{NaK}	Na^+/K^+ pump current
I_{pCa}	plateau calcium current
I_{pK}	plateau potassium current
I_{bNa}	background inward sodium current
I_{bCa}	background inward calcium current

TABLE S2: The various ionic currents in the TP06 model; the symbols used for these currents follow Ref. [4].

II. OUR CONVOLUTIONAL NEURAL NETWORK (CNN)

We give below a brief description about the CNN that we develop. The pseudocolor image \tilde{V} (see the main paper) is fed into the Convolution layer 1 through the input layer. The Convolution layer 1 generates k channels with images that have $m \times n$ pixels from input images of $m' \times n'$ in k' channels (initially $m' = n' = 32$ and $k' = 1$; these images are enlarged by padding (so that there are $(m' + 2p) \times (n' + 2p)$ pixels) and then combined with filters specified by weights $W_{i,j}^{c,c'}$ and the filter-bias b^c as follows:

(v) *O'Hara and Rudy (ORd) model*

I_{Na}	inward sodium current
I_{CaL}	L-type inward calcium current
I_{to}	Transient outward potassium current
I_{Ks}	Slow delayed rectifier outward potassium current
I_{Kr}	Rapid delayed rectifier outward potassium current
I_{K1}	Inward rectifier outward potassium current
I_{NaCa}	Na^+/Ca^{++} exchange current
I_{CaNa}	CaMK activated sodium current
I_{CaK}	CaMK activated potassium current
I_{NaK}	Na^+/K^+ ATPase current
I_{pCa}	calcium pump current
I_{Kb}	background rapidly activating potassium current
I_{Nab}	background sodium current
I_{Cab}	background calcium current

TABLE S3: The various ionic currents in the ORd model; the symbols used for these currents follow Ref. [5].

$$O_{A, i, j}^{c, s} = \sum_{c'=0}^{k-1} \sum_{i', j'=0}^{\gamma-1} \left(I_{s i+i', s j+j'}^{c'} W_{i', j'}^{c, c'} \right) + b^c J_{i, j}, \quad (7)$$

where s is the *stride length*, c' and c are the *channel numbers* of the input and output, respectively, γ is the *filter size*, and $m = \lfloor (m' + 2p - 1)/s \rfloor + 1$, $n = \lfloor (n' + 2p - 1)/s \rfloor + 1$, $i \in \{0, 1, \dots, m-1\}$, $j \in \{0, 1, \dots, n-1\}$, where, for $x \in \mathbb{R}$, $\lfloor x \rfloor$ is the integer part of x , and $J_{i, j} = 1, \forall i, j$.

Next, the output from Eq. (7) is fed to ReLU that clips the negative values as follows:

$$O_{B, i, j}^{c, s} = \max \left\{ 0, O_{A, i, j}^{c, s} \right\}. \quad (8)$$

Then the image from ReLU passes through the MaxPooling layer, which reduces the image size, but preserves its essential features, via the following operation:

$$O_{C,i,j}^{c,s} = \max_{i',j'=0}^{\gamma'-1} \left\{ O_{B,s}^{c,s'} \right\}, \quad (9)$$

where i and j are defined as in Eq. (7) and γ' and s' are, respectively, the *pool size* and the stride length. The operations in Eqs. (7)-(9) are repeated for each set of Convolution, ReLU, and MaxPooling layers (we have 3 such sets in the Middle layer in Fig. S1).

The output from the last MaxPooling layer $O_{C,i,j}^{c,s}$, which is an $m \times n \times k$ array, is converted into a vector $I_{FL,i}$ of size $mnk \times 1$ and then passed to the fully connected layer (ANNs). We use three layers in our ANN, namely: input, hidden, and output layer. From the ANNs we get:

$$O_{D,q} = \tanh \left(\sum_{i'=0}^{mnk-1} (W_{D,q,i'} I_{FL,i'}) + b_{D,q} \right);$$

$$O_{E,q'} = \tanh \left(\sum_{q=0}^{\zeta-1} (W_{E,q',q} O_{D,q}) + b_{E,q'} \right); \quad (10)$$

$$\tilde{O}_q = \frac{\exp(O_{E,q})}{[\sum_{q'=0}^{\eta-1} \exp(O_{E,q'})]}; \quad (11)$$

here $\zeta = 256$ is the number of nodes in the hidden layer of the ANN, η is the number of nodes in the output layer, which corresponds to the number of classes and $q \in \{0, 1, \dots, \eta - 1\}$; in our case $\eta = 2$, and the classes are \mathcal{S} (*spiral waves*) and $\mathcal{N}\mathcal{S}$ (*no spiral waves*).

Initially the weights $W_{i',j'}^{c,c'}$, $W_{FL,i,i'}$, $W_{D,q,i'}$ and $W_{E,q',q}$ are chosen to have random values (from a zero-mean Gaussian distribution with standard deviation 0.01); and the biases b^c and $b_{FL,i}$ are taken to be 0.

We have mentioned in the main paper that our CNN can be used to detect scroll waves in three-dimensional (3D) simulation domains. An illustration of such detection by our CNN, which uses a 2D section through the 3D scroll wave is given in Fig. S4.

III. CONTROL SCHEMES FOR THE ELIMINATION OF UNBROKEN AND BROKEN SPIRAL WAVES

We give here brief overviews of three schemes that we use to control unbroken and broken spiral waves in the mathematical models for cardiac tissue that we have described above. The first is the mesh-control scheme [6–10]; our description here follows that in Ref. [11].

A. Mesh-control scheme

The development of control schemes for the elimination of unbroken and broken spiral waves, in mathematical

models for cardiac tissue, is of great importance in searching for low-amplitude defibrillation methods, for the elimination of life-threatening cardiac arrhythmias, such as ventricular tachycardia (VT) and ventricular fibrillation (VF). The mathematical analogs for these arrhythmias are, respectively, unbroken and broken spiral waves. One such control scheme, which has been very successful in the elimination of such waves in a variety of mathematical models for cardiac tissue [6–10], removes spiral waves by the application of currents on a square mesh. In this scheme, we divide the simulation domain into square cells of dimension $N_G \times N_G$ grid points (given a domain of size $N \times N$ grid points, we must have $N > N_G$); we then apply a stimulus current, of amplitude 50 pA/pF, for 100 ms along the edges of the square cells, as in Ref. [8]; this eliminates spiral wave, as we show in top panel of Fig. S3.

B. Optogenetics-based control scheme:

Optogenetics is an emerging technique that has been used for controlling excitation waves in cardiac tissue. In particular, it has been used for the effective elimination of unbroken and broken spiral waves in *in vitro* and *in silico* studies of cardiac tissue [12–17]. The light-activated ion-channel protein *channelrhodopsin* is expressed in a cell (a cardiac myocyte in our case); and the form and initiation of the action potential of this cell can be controlled through optical stimulation. In simulation studies, channelrhodopsin is modelled by a four-state, Markov-chain model as shown in Fig.S2. The equations governing these states, their rates, and the current through this channel are given in Eqs. (4)-(9) (see, e.g., Ref. [18]). In our optogenetics-based control scheme for the mathematical models of cardiac tissue that we study, we express the channelrhodopsin in cardiac myocytes, at random positions in the tissue, such that the percentage of modified cardiac myocytes is P_f . When our CNN detects an unbroken or broken spiral wave (the class \mathcal{S} in the main paper) at some time in our numerical simulation, we activate the channelrhodopsin by irradiating the tissue with light of strength 15 mW/mm² for a duration of $\simeq 10 - 15$ ms. In bottom panel of Fig. S3, we illustrate the elimination of such waves, via this optogenetics-based method, for the LR-I model; we obtain similar results for the TP06 and ORd models. The values of P_f and the irradiation strength are crucial control parameters in the elimination of spiral waves. In our study we use $P_f = 15\%$, which is the minimum value that leads to successful control.

C. Gaussian-control scheme applied in LR-I and AP models

In the main paper, we have used the Gaussian-control scheme to eliminate spiral waves in the TP06 model. We show, in Fig. S6 and Fig. S5, respectively, that this scheme also removes broken spiral waves in the AP and

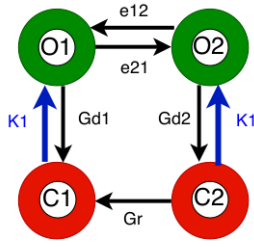


FIG. S2: A schematic diagram showing the Markov-chain model for *channelrhodopsin*; this consists of two closed states (C1,C2) and two open states (O1,O2). The rate $K1$ depends on the strength of the irradiation [13].

LR-I models.

$$I_{ChR2} = g_{ChR2}G(V)(O_1 + \gamma O_2)(V - E_{ChR2}); \quad (12)$$

$$O_1 + O_2 + C_1 + C_2 = 1; \quad (13)$$

$$\frac{dC_1}{dt} = G_r C_2 + G_{d1} O_1 - k_1 C_1; \quad (14)$$

$$\frac{dO_1}{dt} = k_1 C_1 - (G_{d1} + e_{12}) O_1 + e_{21} O_2; \quad (15)$$

$$\frac{dO_2}{dt} = k_2 C_2 - (G_{d2} + e_{21}) O_2 + e_{12} O_1; \quad (16)$$

$$\frac{dC_2}{dt} = G_{d2} O_2 - (k_2 + G_r) C_2; \quad (17)$$

$$k_1 = \phi_1(F, t) = \epsilon_1 F p; \quad (18)$$

$$k_2 = \phi_2(F, t) = \epsilon_2 F p; \quad (19)$$

$$F = \sigma_{ret} I \frac{\lambda}{(w_{loss} hc)}; \quad (20)$$

$$\frac{dp}{dt} = \frac{(S_0(\theta) - p)}{\tau_{ChR2}}; \quad (21)$$

$$S_0(\theta) = 0.5(1 + \tanh(120(\theta - 0.1))); \quad (22)$$

$$G(V) = \frac{(10.6408 - 14.6408 e^{(-\frac{V}{42.7671})})}{V}; \quad (23)$$

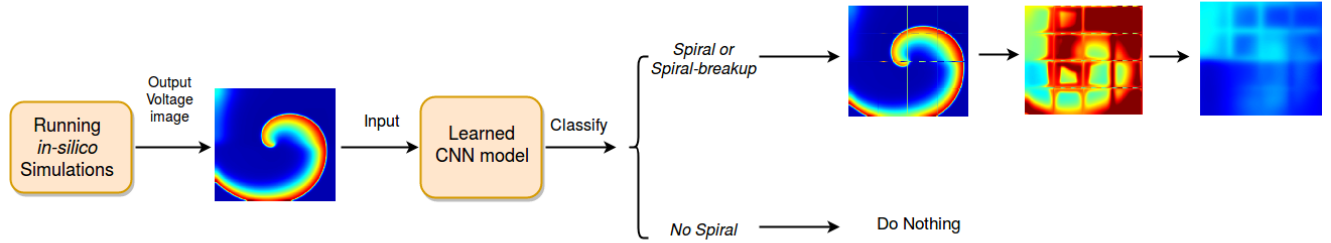
$$G_{d1} = 0.075 + 0.043 \tanh(-\frac{(V + 20)}{20}); \quad (24)$$

$$G_r = 4.34 \times 10^5 e^{-(0.0211539274 V)}. \quad (25)$$

-
- [1] Dwight Barkley. A model for fast computer simulation of waves in excitable media. *Physica D: Nonlinear Phenomena*, 49(1-2):61–70, 1991.
- [2] Rubin R Aliev and Alexander V Panfilov. A simple two-variable model of cardiac excitation. *Chaos, Solitons & Fractals*, 7(3):293–301, 1996.
- [3] Ching-hsing Luo and Yoram Rudy. A model of the ventricular cardiac action potential. depolarization, repolarization, and their interaction. *Circulation research*, 68(6):1501–1526, 1991.
- [4] Kirsten HWJ Ten Tusscher and Alexander V Panfilov. Alternans and spiral breakup in a human ventricular tissue model. *American Journal of Physiology-Heart and Circulatory Physiology*, 291(3):H1088–H1100, 2006.

- [5] Thomas O’Hara, László Virág, András Varró, and Yoram Rudy. Simulation of the undiseased human cardiac ventricular action potential: model formulation and experimental validation. *PLoS computational biology*, 7(5):e1002061, 2011.
- [6] T.K. Shajahan, S. Sinha, and R. Pandit. Spiral-wave dynamics depend sensitively on inhomogeneities in mathematical models of ventricular tissue. *Phys. Rev. E*, 75(1):011929, 2007.
- [7] TK Shajahan, Alok Ranjan Nayak, and Rahul Pandit.

Case (i) Mesh-control scheme



Case (ii) Optogenetics-based control scheme

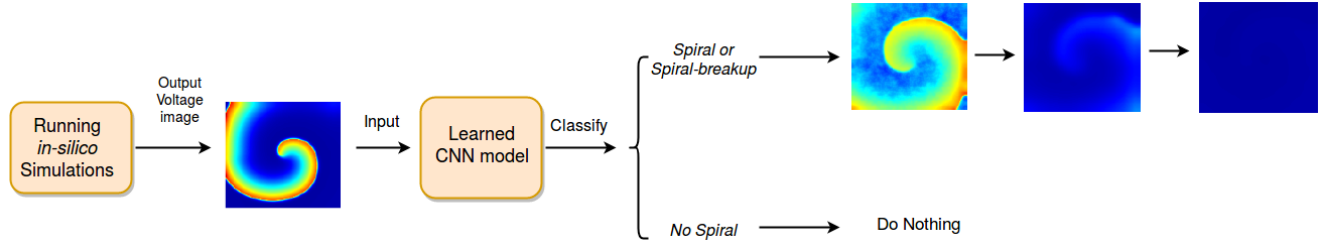


FIG. S3: Schematic figures, top and bottom panels, showing the detection of spiral waves by our trained CNN model and, thereafter, the elimination of these waves by mesh-control and optogenetics-based-control schemes for the illustrative case of the LR-I model.

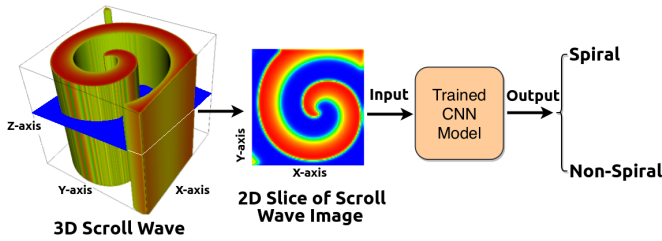


FIG. S4: An illustration of the detection of a scroll wave by our CNN, which uses a two-dimensional (2D) section through the three-dimensional (3D) scroll wave; .

Spiral-wave turbulence and its control in the presence of inhomogeneities in four mathematical models of cardiac tissue. *PLoS One*, 4(3):e4738, 2009.

- [8] Sitabhra Sinha, Ashwin Pande, and Rahul Pandit. Defibrillation via the elimination of spiral turbulence in a model for ventricular fibrillation. *Physical review letters*, 86(16):3678, 2001.
- [9] R. Pandit, A. Pande, S. Sinha, and A. Sen. Spiral turbulence and spatiotemporal chaos: characterization and control in two excitable media. *Physica A: Statistical Mechanics and its Applications*, 306:211–219, 2002.
- [10] A.R. Nayak and R. Pandit. Spiral-wave dynamics in ionically realistic mathematical models for human ventricular tissue: the effects of periodic deformation. *Frontiers in Physiology*, 5:207, 2014.
- [11] Mahesh Kumar Mulimani, Alok Ranjan Nayak, and Rahul Pandit. Comparisons of wave dynamics in hodgkin-huxley and markov-state formalisms for the sodium (na) channel in some mathematical models for human cardiac tissue. *arXiv preprint arXiv:1811.09501*, 2018.
- [12] Tobias Bruegmann, Daniela Malan, Michael Hesse, Thomas Beiert, Christopher J Fuegemann, Bernd K Fleischmann, and Philipp Sasse. Optogenetic control of heart muscle in vitro and in vivo. *Nature methods*, 7(11):897, 2010.
- [13] Patrick M Boyle, John C Williams, Christina M Ambrosi, Emilia Entcheva, and Natalia A Trayanova. A comprehensive multiscale framework for simulating optogenetics in the heart. *Nature communications*, 4:2370, 2013.
- [14] Brian O Bingen, Marc C Engels, Martin J Schalijs, Wanchana Jangsangthong, Zeinab Neshati, Iolanda Feola, Dirk L Ypey, Saïd FA Askar, Alexander V Panfilov, Daniël A Pijnappels, et al. Light-induced termination of spiral wave arrhythmias by optogenetic engineering of atrial cardiomyocytes. *Cardiovascular research*, 104(1):194–205, 2014.
- [15] Christina M Ambrosi, Aleksandra Klimas, Jinzhu Yu, and Emilia Entcheva. Cardiac applications of optogenetics. *Progress in biophysics and molecular biology*, 115(2-3):294–304, 2014.
- [16] Patrick M Boyle, Thomas V Karathanos, Emilia Entcheva, and Natalia A Trayanova. Computational modeling of cardiac optogenetics: Methodology overview & review of findings from simulations. *Computers in biology and medicine*, 65:200–208, 2015.
- [17] Rupamanjari Majumder, Iolanda Feola, Alexander S Teplenin, Antoine AF de Vries, Alexander V Panfilov, and Daniel A Pijnappels. Optogenetics enables real-time spatiotemporal control over spiral wave dynamics in an excitable cardiac system. *eLife*, 7:e41076, 2018.
- [18] John C Williams, Jianjin Xu, Zhongju Lu, Aleksandra Klimas, Xuxin Chen, Christina M Ambrosi, Ira S Cohen, and Emilia Entcheva. Computational optogenetics: empirically-derived voltage-and light-sensitive

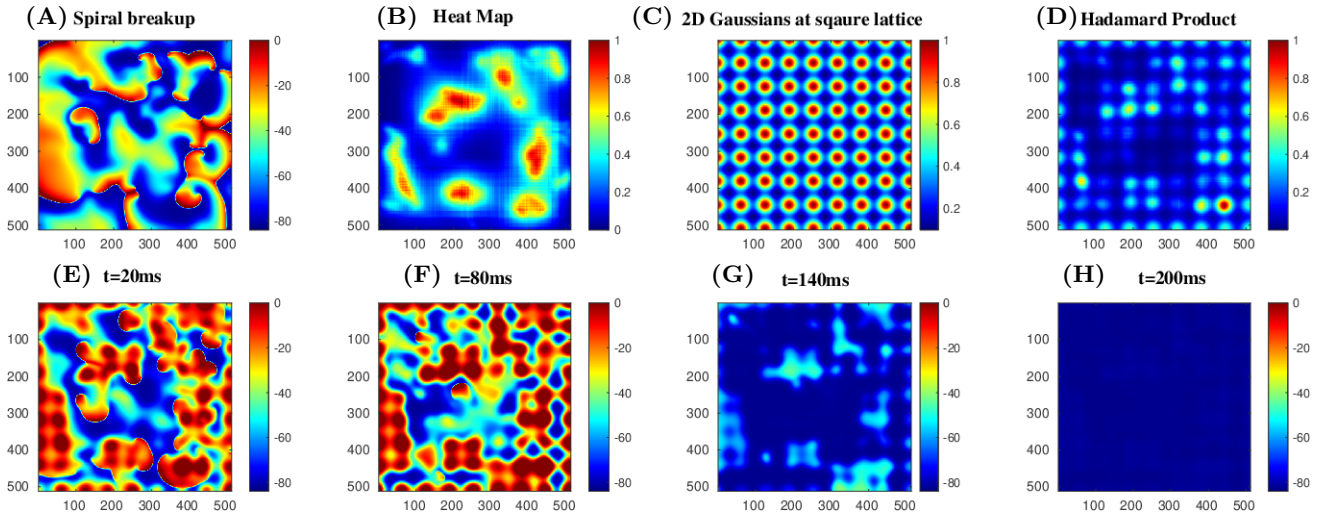


FIG. S5: Gaussian-control scheme; LR-I model. Pseudocolor plots (A) of V (showing broken spiral waves), (B) the corresponding heat map generated by using our CNN (main paper), (C) 2D Gaussians with $\sigma = 0.496$ cm, (D) the Hadamard product $\mathcal{P}_{\mathcal{H}}(i, j)$ of 2D Gaussians on a square lattice with the heat map (main paper). (E)-(H) Pseudocolor plots of V , at different instants of time t showing how our Gaussian-control scheme (with $I_{def} = 5$ pA/pF and $t_{def} = 100$ ms) eliminates broken spiral waves.

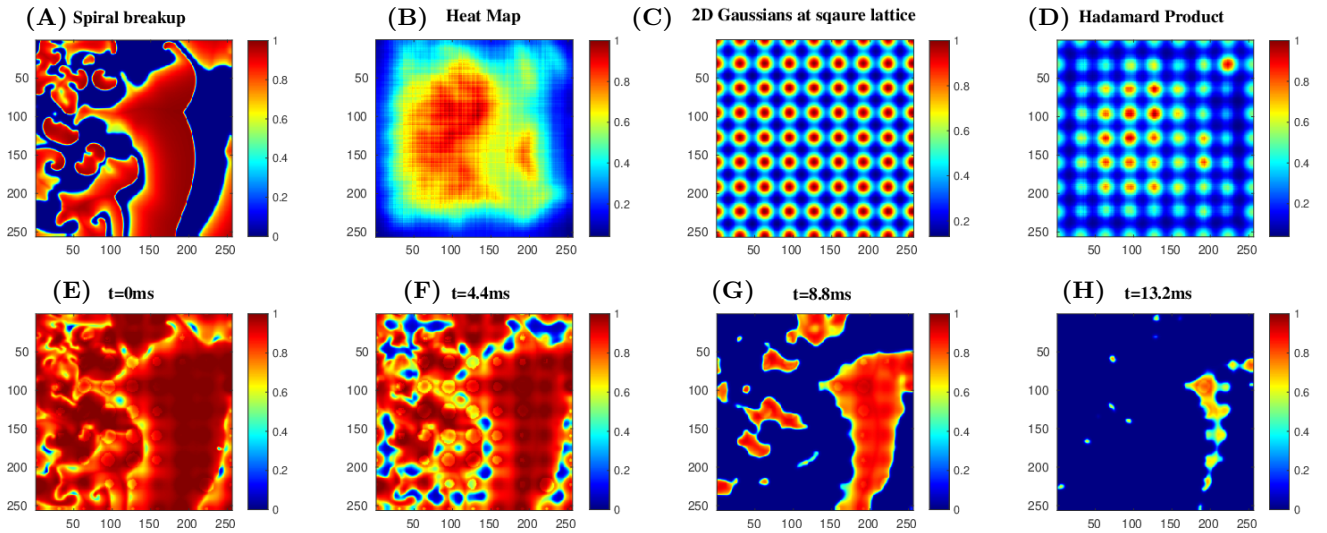


FIG. S6: Gaussian-control scheme; AP model. Pseudocolor plots (A) of V (showing broken spiral waves), (B) the corresponding heat map generated by using our CNN (main paper), (C) 2D Gaussians with $\sigma = 0.496$ cm, (D) the Hadamard product $\mathcal{P}_{\mathcal{H}}(i, j)$ of 2D Gaussians on a square lattice with the heat map (main paper). (E)-(H) Pseudocolor plots of V , at different instants of time t showing how our Gaussian-control scheme (with $I_{def} = 1.4$ pA/pF and $t_{def} = 6.6$ ms) eliminates broken spiral waves.

channelrhodopsin-2 model. *PLoS computational biology*, 9(9):e1003220, 2013.